Prediction-driven Respiratory Motion Atlas Formation for 4D Image-guided Radiation Therapy in Lung

Xiaoxiao Liu[1], Bradley C. Davis[2], Marc Niethammer[1], Stephen M. Pizer[1], Gig S. Mageras[3]

[1] Department of Computer Science, University of North Carolina at Chapel Hill, NC
[2] Kitware, Inc., Clifton Park, NY
[3] Department of Medical Physics, Memorial Sloan-Kettering Cancer Center, New York, NY

Abstract. Respiratory motion challenges lung radiation therapy with uncertainties of the location of important anatomical structures in the thorax. To capture the trajectory of the motion, dense image matching methods and learning-based motion prediction methods have been commonly used. However, both methods have limitations. Serious motion artifacts in treatment-guidance images, such as streak artifacts in respiration-correlated cone-beam CT, challenge the intensity-based image matching; the learning-based prediction methods require consistency between the training data for planning and the data for treatment. This paper proposes a prediction-driven motion atlas framework for motion estimation with artifact-laden images, using a Fréchet-mean-image matching scheme that is softly constrained by deformation predictions. In this framework, all the respiration phase-stamped images within a breathing cycle are diffeomorphically deformed to their Fréchet mean. The iterative optimization is driven by both intensity matching forces and the prediction forces trained from patient-specific planning images. The effectiveness of the framework is demonstrated with computational phantom and real cone-beam CT images.

1 Introduction

Positional uncertainties caused by the respiratory motion have been shown to have a large impact on radiation dose [1]. Accurate respiratory motion estimation is necessary for removing the motion-induced uncertainties. Cone-beam CT (CBCT) exploits flat panel technology to integrate the imaging system directly into the treatment accelerator, allowing acquisition of a volumetric image at each respiratory phase in the treatment position and eliminating the need for marker implantation [2–4]. A major limitation of CBCT systems is image degradation caused by respiration-induced motion, which compromises tumor and organ-at-risk localization for guiding radiation treatment of cancer. The work presented here is part of a larger project to correct respiratory motion-induced artifacts

in CBCT scans [4]. Briefly, CBCT projection images are sorted into subsets according to a respiration signal and reconstructed to obtain a set of low-quality respiration-correlated CBCT images. Application of nonrigid registration deforms each of the respiration-correclted CBCT (RC-CBCT) images to a chosen reference image in the set; combining all images yields a single high-quality CBCT image with reduced blurring and motion artifacts. However, degradation of image quality resulting from the sparse projections for each subset in the filtered back-projection reconstructions imposes serious limitations on non-rigid image registrations. The fourth dimension of the "4D" notion in this paper refers to the respiration phase during one breathing cycle.

Two different categories of methods have been used to capture the respiratory motion trajectory. One is ordinary intensity-based image matching or tracking. Various non-linear dense image registrations can be used to calculate the spatial changes of each voxel between images by matching their intensity profiles [5, 6]. However, the image registration could easily get trapped in local minima when imaging artifacts are present and thus tends to over-fit to those artifacts.

The other category is linear motion modeling with surrogate signals. Recognizing the hysteresis of respiration, various external and internal surrogate signals have been used for motion modeling and prediction in lung. The diaphragm position of the lung has been used as a navigator of the image deformation and used for motion prediction for CBCT-guided radiation therapy [7, 4]. Recently, the shape of the lung has been used as an advanced surrogate for motion prediction, in which the so-called *shape-correlated deformation statistics* (SCDS) reveals the maximum linear correlations between the shape surrogates and the image deformations [8, 9]. The SCDS is trained on a prior respiration-correlated CT (RCCT) set acquired for treatment planning purposes. The RCCT consists of a sequence of volumetric CT images over the breathing cycle.The underlying assumption of any surrogate-involved learning-based model that uses a prior image set is that the correlation between the surrogate and the underlying motion are the same for both planning/training time and treatment/test time. The assumption simplifies the complicated breathing system and justifies the estimation by directly incorporating the training information. However, the correlations between the surrogate and the spatial deformation cannot be exactly the same, especially for cancer patients who have difficulty in stabilizing their breathing over time. Besides, noise kept in the SCDS trained from few planning phases tend to result in local region prediction errors.

To fully utilize both categories of methods while avoiding their limitations, in this paper we combine the intensity information (from the treatment RC-CBCT) and the SCDS-predictions (from the planning RCCT) into a unified framework for improved motion estimation. On the one hand, the motion prediction can help regularize the intensity matching from over-fitting. On the other hand, meaningful image features can be utilized to reduce prediction errors.

A respiratory motion atlas formation method driven by a combination of prediction matching forces and image matching forces is developed in this paper. A respiratory motion atlas contains an atlas image and the dense image

deformations that transform each phase-stamped image in the breathing cycle to the atlas image. Instead of an image at an arbitrary time point, a Fréchet mean image that takes the minimum total amount of transformations to match all images is computed and used as the atlas image for increased robustness. The deformations predicted from a shape-correlated deformation statistics (SCDS) model are used as a soft constraint during the optimization. The balancing force between the intensity force and the prediction force can be adjusted via a weighting factor, selected upon the credibility of the training statistics and the quality of the treatment images.

The rest of the paper is organized as follows. Section 2 introduces the framework of the proposed prediction-driven deformation atlas formation. Specifically, section 2.1 introduces the Fréchet mean image formation method that is used to obtain the respiratory motion atlas from a 4D image sequence; section 2.2 presents the techniques that are used to apply trained SCDS to predict motion from a noisy 4D image sequence; Section 2.3 introduces the prediction-driven atlas formation by integrating the SCDS-predictions into the Fréchet mean formation framework. Experimental results are presented in Section 3.

2 Methodology

2.1 Respiratory Fréchet mean image formation

To quantify the breathing motion from a 4D image sequence, non-linear dense image registrations are often used to compute the spatial changes for each voxel in the image. The breathing motion can be quantified by the non-linear deformations that match each phase-stamped image in the breathing cycle to an atlas image. The atlas image, together with the deformations, form the respiratory motion atlas for this patient. For the respiration-correlated CT (RCCT) that is used at the planning time in IGRT, the high-contrast and good image resolution enables intensity-based registration methods to accurately capture the spatial changes over the breathing cycle.

There are several aspects to be considered in choosing a proper atlas image. First of all, due to the large anatomical variations between patients, it is more practical for the atlas image to be patient-specific. Secondly, to be used for motion prediction, the conformation of the atlas image should also be stable over time or at least stable between the planning time and the treatment or target time. The end expiration (EE) phase is commonly used as the reference phase for registration due to its relatively stable repeatability. However, computationally, a smaller total amount of deformations is preferred for better image registration accuracy and efficiency. Further, in order to carry out statistical analysis on the deformations (for SCDS calculation in Section 2.2), an "averaged" atlas will help to get tightest statistical distribution.

A Fréchet mean image has the property that it minimizes the sum of squared distances on the Riemannian manifold of diffeomorphic transformations to a group of images (see Figure 1). It represents an averaged spatial configuration

of that group [10]. Therefore, the Fréchet mean image of the breathing sequence well satisfies the aforementioned criteria and is used in this paper as the atlas image.
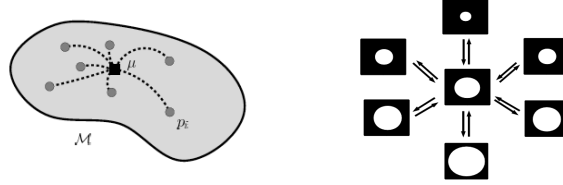

Fig. 1: Fréchet image mechanism: a) The filled circles represent individual points $\mathbf{p}^i$ on the Riemannian manifold $\mathcal{M}$. The Fréchet mean (filled square) is the point μ on the manifold that minimizes the sum of squared distances to the observations. Distances are measured along the manifold; b) Iterative Fréchet mean image construction framework illustrated on images of spheres with varying radius. The mean image in the middle minimizes the sum of squared deformation distances required to match all input images.

Given a group of phase-stamped images, geometric changes over time are represented as the action of a group of diffeomorphisms on images. Let $\mathrm{Diff}_V(\Omega)$ be the group of diffeomorphisms that are isotropic to the identity. An element $\phi : \Omega \to \Omega$ in $\mathrm{Diff}_V(\Omega)$ deforms an image I to the image $I \circ \phi$. The geodesic distance between a pair of images on the manifold is defined by diffeomorphic matching:

$$d^2(I^F, I^M) = \mathrm{argmin} \int_0^1 ||v_t||_V^2 dt + \frac{1}{\sigma^2}||I^M \circ \phi - I^F||_{L2}^2, \tag{1}$$

subject to $\phi(x) = x + \int_0^1 v_t dt$, where $t \in [0,1]$. The first term defines a metric on the space of diffeomorphisms that are generated by integrating velocity fields v. These diffeomorphisms are used to deform a moving image I^M (image at $t = 0$) to match a fixed image I^F (image at $t = 1$). The second term penalizes residual image dissimilarity. The parameter σ controls the relative weight of these terms.

The Fréchet mean $\hat{I}$ is the image that requires the least amount of deformation to map onto the group of input images I^i: $\hat{I} = \mathrm{argmin} \sum_{i=1}^N d(I, I^i)^2$. Combined with geodesic distance definition (1), the optimization problem can be summarized as

$$\hat{I}, \hat{\phi}^i = \underset{I,\hat{\phi}^i \in \mathbb{I} \times \mathrm{Diff}_V(\Omega)^N}{\mathrm{argmin}} \sum_{i=1}^N \left[\int_0^1 ||v_t^i||_V^2 dt + \frac{1}{\sigma^2}||I - I^i \circ \phi^i||_{L2}^2 \right],$$

subject to $\phi_0^i = Id$, $\phi^i(x) = x + \int_0^1 v_t^i(\phi_t^i(x))dt$.

Initialized with identity transformations, an iterative optimization updates the Fréchet mean image at each iteration, and the deformations that transform all the phases to the Fréchet mean are optimized at the same time.

2.2 SCDS-based prediction

The shape-correlated deformation statistics (SCDS) model has been shown to effectively reveal the patient-specific linear correlations between the shape surrogates and the image deformations [8, 9]. In this method, the shape of the lung is used as an internal surrogate signal to navigate the dense image deformation by linear regression. The shape models are extracted using lung surface segmentation from the images followed by application of an entropy-based particle system [11] to obtain a group-wise surface correspondence over the phases within the breathing cycle. The SCDS model trained from the planning images is used to predict the motion of the images via extracted shape surrogates.

In previous papers [8, 9], the SCDS model used the EE phase as the image atlas. In this paper, we improve the tightness of the SCDS by using the Fréchet mean as the image atlas. Also we use deformable segmentation techniques to apply the SCDS for motion prediction to CBCT images with image artifacts. The resulting predicted deformations are going to be used as soft constraints in the overall prediction-driven atlas framework described in Section 2.3.

Probabilistic deformation segmentation To apply this method to CBCT images, robustly extracting the lung boundaries against the streak intensity artifacts is important. We have developed a posterior probability optimization scheme to calculate the models that fit into the target images while staying in the trained shape space. The optimization is described in

$$\mathbf{log}\ p(\mathbf{q}^i|J^i) = \underset{q^i}{\mathrm{argmax}}[\mathbf{log}\ p(J^i|\mathbf{q}^i) + \mathbf{log}\ p(\mathbf{q}^i)], \tag{2}$$

where $\mathbf{q}^i$ is the deformable surface mesh (to distinguish the shapes $\mathbf{p}^i$ in training) segmented from the CBCT image J^i (to distinguish the training image I^i). The image match term or the likelihood term is the summation of a second-order gradient magnitude measured on the surface of the model, indicating how well the model fits to the boundaries. The prior term is measured by Mahalanobis distance of the model from the training mean in the trained shape space.

SCDS-prediction for 4D CBCT In the motion atlas, the deformation of the whole dense deformation field is represented by the displacement vector field (DVF) u as the result of the diffeomorphic transformation from each phase image to the atlas image. To distinguish the planning data and the treatment data, in this paper ϕ^i denotes the deformations calculated from RCCT images I^i and φ^i denotes the deformations calculated from RC-CBCT images J^i. It follows that

$\mathbf{u}_\varphi$ denotes the DVFs from RCCTs and $\mathbf{u}_\varphi$ denotes the DVFs from RC-CBCT. In summary, three major steps are carried out to estimate the image deformations in 4D CBCT.

1. The DVFs $\mathbf{u}_\phi^i$ of RCCTs are obtained by the intensity-based Fréchet mean formation method introduced in the last section. The surface models of the lung are extracted from each CT phase images. The linear correlation $\mathbf{C}$ that maps a shape surrogate $\mathbf{p}^i$ to its corresponding image deformation $\mathbf{u}_\phi^i$ is calculated such that $\mathbf{u}_\phi = \mathbf{C} \cdot \mathbf{p} + \epsilon$, where ϵ is the regression error.
2. The lung shape $\mathbf{q}^i$ is segmented from the CBCT images J^i using the posterior probability optimization scheme.
3. Deformations of each time-point of the CBCT sequence $\mathbf{u}_\varphi^i$ are calculated by $\mathbf{u}_\varphi^i = \mathbf{C} \cdot \mathbf{q}^i$.

After the motion prediction, an atlas image can be calculated by averaging all the intensity images after warping them using the predicted deformations.

2.3   Prediction-driven respiratory motion atlas formation

The SCDS-prediction method is a learning-based approach that is resistant to image artifacts. However, as mentioned in the introduction, its accuracy also depends on the *correlation consistency* condition of the motion between the training data and the target data. For lung cancer patients who themselves have difficulties to strictly regularize their breathing patterns or as a result of anatomical changes such as tumor growth, the correlation between the surrogate lung and the overall image deformation can not be exactly the same. Besides, the linear correlation regression results contain statistics errors due to the high dimensional low sample size (HDLSS) problem.

To increase the prediction robustness of the method, image intensity features can be used to adapt to the motion variations between the training and the testing data. Despite the CBCT artifacts, there are still many intensity features (besides the lung boundaries) useful for guiding the image registration, such as the bony rib cage, the bronchial structures, and the tumor region itself.

A prediction-driven deformation atlas formation method, optimized by the combination of prediction constraints and image matching forces is presented here to improve the motion estimation accuracy and robustness. The deformation predictions are used as soft constraints in the iterative Fréchet mean image optimization, as follows:

$$\hat{J}, \hat{\varphi}^i = \underset{J,\hat{\varphi}^i}{\text{argmin}} \sum_1^N \left[\int_0^1 ||v_t^i||_V^2 dt + \frac{1}{\sigma_1^2}||J - J^i \circ \varphi^i||_{L2}^2 + \frac{1}{\sigma_2^2} d_R^2(\varphi^i, \phi^i(q^i)) \right],$$

subject to $\varphi^i = x + \int_0^1 v_t^i dt$, where J^i denotes the CBCT image at phase i, $\hat{J}$ is the atlas image and $\mathbf{q}^i$ is the lung shape segmented from J^i using the deformable segmentation method introduced in Section 2.2. The distance between the varying deformation φ^i and the prediction $\phi(q^i)$ is measured via the Riemannian

manifold metric d_R, which is defined as the minimum of the integral over all piecewise smooth curves that connect ψ_1 and ψ_2. This distance can be alternatively computed by $d_R(\psi_1 \circ \psi_2^{-1}, id)$, where id is the identity transformation.

To simplify the computation and to directly use the resulting deformation represented by DVFs (deformations from the atlas image) computed from the SCDS-prediction, an Euclidean approximation of the square Riemannian distance is given by $d_R^2(\varphi^i, \phi(q^i)) \approx ||\mathbf{u}_{\varphi^i} - \mathbf{u}_{\phi(\mathbf{q}^i)}||_{L^2}^2$, where the SCDS-predicted deformation $\mathbf{u}_{\phi(\mathbf{q}^i)}$ is computed by linear mapping $\mathbf{u}_{\phi(\mathbf{q}^i)} = \mathbf{C} \cdot \mathbf{q}^i$. The Euclidean deformation space is only an approximation of the Riemannian deformation manifold. However, when deformations are not very large, the Euclidean space can be thought of as the tangent plane of the Riemannian manifold at the Fréchet mean and thus the linear approximation is sufficient.

The balancing force between the prediction and the noisy intensity profile can be adjusted via the weighting factors σ_1 and σ_2, selected upon the credibility of the training statistics and the quality of the treatment images. To have equal influences from both the intensity and the prediction, the weighting factors should make the two energy terms have the same order of magnitude. The energy term of the prediction is treated as an extra feature channel.

Computationally, this extra channel itself is a three-dimensional-vector channel and takes three times the storage as the image intensity. In comparison to the intensity-based atlas method, the prediction-driven atlas method takes more time to compute the gradient for the extra prediction constraints. On the other hand, due to the prediction constraints fewer iterations are typically required for convergence.

3   Experimental results

3.1   Breathing spheres

We started with some simulation data to test the prediction-driven atlas formation method. A sequence of sphere images with varying radii were designed to mimic the breathing scenario. The radii follow a sinusoidal curve to simulate the breathing pattern of a volume enlarging process followed by a volume shrinking. The surface points on the spheres (not shown) are used as the shape surrogate to carry out the SCDS motion prediction. With the same dateset, Gaussian noise is added to create the test data, as shown in Figure 2a.

The underlying correlation between the shape surrogate, the surface point set sampling on the spheres with group-wise correspondence, and the image deformation are the same for the training and the testing data, since the only difference between the two datasets is the added Gaussian noise. It is shown that the intensity-based atlas formation method (Figure 2c) tends to over-fit the noise, while the SCDS-prediction (Figure 2d) that is determined by the training SCDS shows resistance to the noise and gives better results.

To simulate variations in the correlations between the training set and the test set, the correlation coefficients between the shape surrogate (surface point
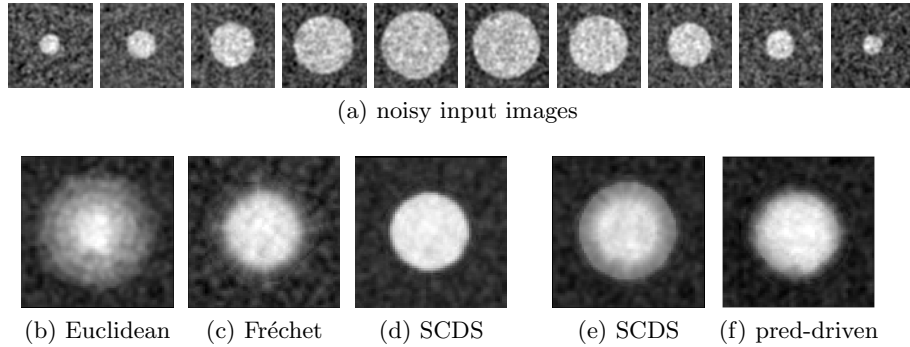
(a) noisy input images

(b) Euclidean   (c) Fréchet   (d) SCDS   (e) SCDS   (f) pred-driven

Fig. 2: **Noisy breathing spheres test**: a) The noisy test image sequence. b) The Euclidean mean of the noisy test sequence. c) The Fréchet mean image of the test data using the intensity-based atlas formation method. d) The resulting atlas image of SCDS motion prediction. **Test with correlation perturbations**: e) The resulting atlas image of SCDS motion prediction with correlation perturbations; f) The prediction-driven atlas image with correlation perturbations.

(a) DVF (image deformation) error
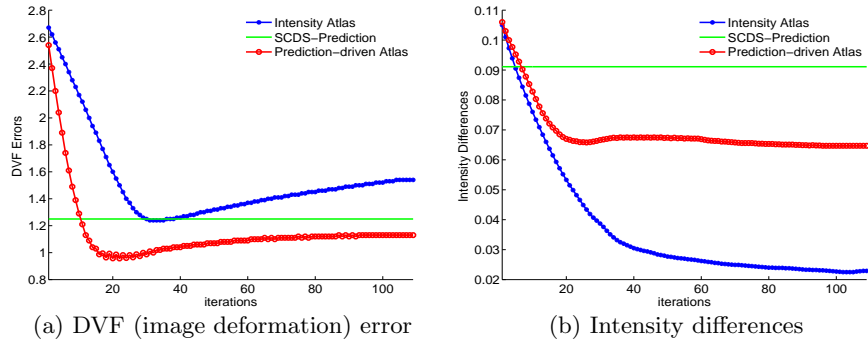

(b) Intensity differences

Fig. 3: Noisy spheres with correlation perturbations: a) Average displacement vector field error per voxel at each iteration. b) Average image intensity difference per voxel at each iteration.

set of the sphere) and the image deformations were perturbed randomly by 0.15 at maximum. The SCDS prediction is influenced by the artificial perturbation and produces errors mostly visible at the edge of the atlas sphere (Figure 2e). On the other hand, it is shown that the prediction-driven deformation is able to balance between the intensity force and the prediction force thus getting the best result (Figure 2f). Errors and intensity energies are shown at each iteration step in Figure 3 for a detailed investigation. The intensity-based matching over-fits the noise: intensity differences diminish with iteration but DVF error increases.

Since the SCDS-prediction is directly computed without iterative optimizations, it is shown as the constant value line for comparison. The best estimation result (i.e., lowest DVF error) is achieved by the prediction-driven atlas formation method.

3.2 NCAT data

4D Nurbs-based Cardiac-Torso (NCAT) phantom thorax RCCTs were produced [12] at 10 phases sampled in one breathing cycle. A corresponding RC-CBCT sequence was simulated from the NCAT RCCTs using the protocol of a gantry-mounted KV on-board imaging system [3] that is used in patient radiation therapy guidance. An example image pair is given in Figure 4. Note the strong artifacts in the phase-sorted CBCT caused by the sparse and unevenly spaced projections. The image grid for each image is $512 \times 512 \times 100$, with voxel size of 0.742 mm $\times$ 0.742 mm $\times$ 1.52 mm. Figure 4 shows an example of the NCAT CT and CBCT image and the surface lung shape model.

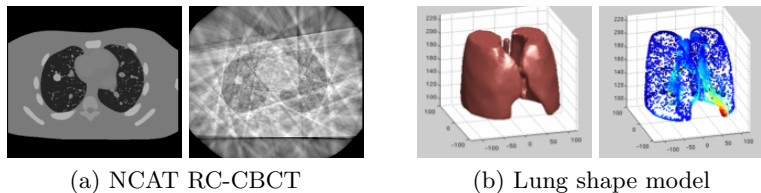(a) NCAT RC-CBCT   (b) Lung shape model

Fig. 4: a) An axial slice of a NCAT RCCT image at EE phase and its corresponding RC-CBCT image. b) The surface mesh representation of the shape of lungs extracted from NCAT RCCTs. The color shows the magnitude of the spatial variation of each point during the breathing cycle.

To test the prediction-driven atlas formation method, inconsistency of the breathing correlation patterns between the training data and the test data were simulated by adding random perturbations into the SCDS-predicted DVFs. The NCAT data set in Figure 5 has a maximum of 2.0 cm diaphragm motion and 0.5 cm anterior-posterior motion. The intensity-based atlas formation results, the SCDS motion prediction results and the prediction-driven atlas formation results are compared in terms of the center of gravity (COG) location errors of the tumor region (Figure 5a). The intensity-based atlas performs better than the SCDS-prediction in terms of the tumor region estimation. The reason is that the tumor region after the CBCT reconstruction has a quite strong contrast respect to its surrounding tissue despite the global streak artifacts. The overall DVF errors of the three methods are compared in Figure 5b. The SCDS-prediction performs better than the intensity-based atlas method. The prediction-driven atlas method shows a compromised overall DVF estimation between the other

two as a result of the combination. These measurements are confirmed from the visual comparison of the atlas images in Figure 6. The prediction-driven atlas (Figure 6c) has less global signal-to-noise ratio (SNR) compared to the intensity atlas (Figure 6a) and has a sharper tumor boundary than the SCDS-prediction atlas (Figure 6b).
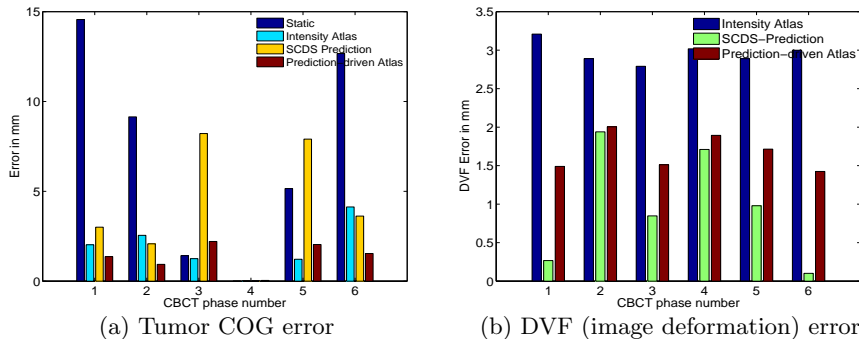

(a) Tumor COG error   (b) DVF (image deformation) error

Fig. 5: a) Tumor COG estimation errors, with the static measurement indicating the mobility of the tumor. The fourth phase is used as the base phase to propagate the tumor contour to other phases. b) DVF estimation error per voxel. The ground truth DVF is obtained by linear interpolation from the RCCT DVFs.

3.3 Patient data

RCCT data sets are provided by a 8-slice scanner, acquiring repeat CT images for a complete respiratory cycle at each couch position while recording patient respiration. The CT images are retrospectively sorted to produce a series of 3D images at 10 respiratory phases. The RC-CBCT scans of five-minute duration are acquired using a slowing-rotating gantry-mounted KV on-board imaging system. The scan produces 3D images at 6 respiratory time points. The image grid for each image is $196 \times 196 \times 100$, with voxel size of 1.52 mm $\times$ 1.52 mm $\times$ 1.52 mm.

Motion estimation results are evaluated on a mock tumor region as shown in Figure 7. Manual segmentations are provided for each CBCT image for error measurements. The manual tumor contour of the fourth phase image (the end-expiration phase) is propagated to all the other phases. The three methods are compared in terms of the COG location errors, see Figure 7. The average COG errors of the 5 phases for the three approaches are 3.5 mm, 2.3 mm and 1.7 mm respectively. The prediction-driven atlas method outperforms the other two approaches in this patient.

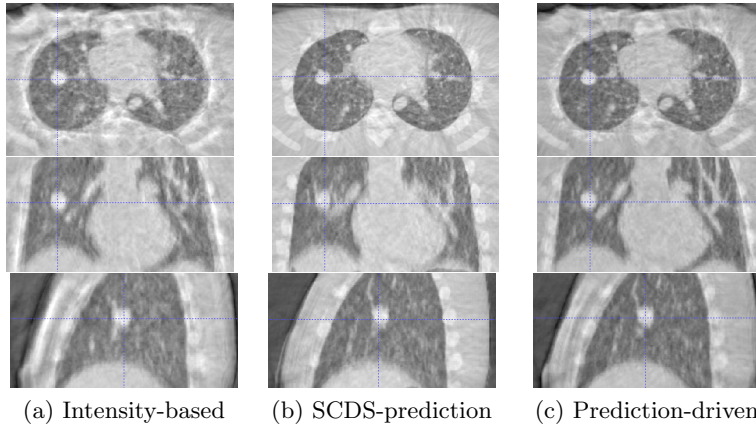(a) Intensity-based   (b) SCDS-prediction   (c) Prediction-driven

Fig. 6: Atlas image comparison of NCAT data set tests. The axial (the first row), coronal (the second row) and sagittal (the third row) slices are compared. a) The Fréchet mean atlas image of the CBCT sequence. b) The atlas image from the SCDS-prediction results. c) The atlas image from the prediction-driven atlas formation method.
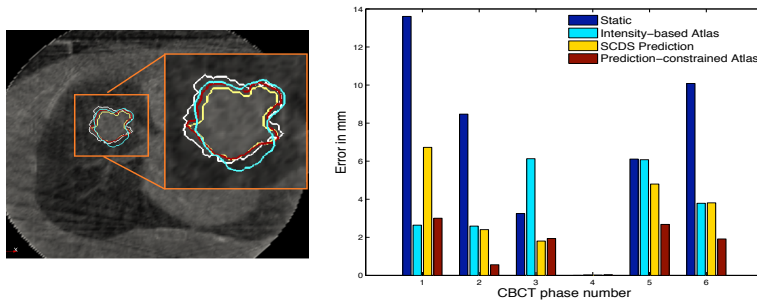

Fig. 7: Left: Axial slices of tumor contours at the fifth phase from the three methods, with the same color legend used in the bar plot on the right. The manual segmentation is shown in white. Right: The comparison of tumor COG errors.

4   Conclusion

The prediction-driven atlas formation framework has the advantage of utilizing high-contrast intensity information from CBCT while being constrained by the shape-correlated prediction results. The overall image deformation result is a compromise between the pure-intensity-based atlas formation method and the SCDS-prediction results, and the structures that have relatively higher contrast contribute to a more accurate local motion estimations. With our preliminary studies on both simulated phantom data and cone-beam CT data, the

prediction-driven atlas method is shown to be more robust for modeling and estimating sophisticated respiratory motion in lung than both the intensity-based atlas method and the learning-based SCDS prediction. More comprehensive validations on patient data are needed to quantify the robustness of the method.

References

1. Minohara, S., Kanai, T., Endo, M., Noda, K., Kanazawa, M.: Respiratory gated irradiation system for heavy-ion radiotherapy. Int J Radiat Oncol Biol Phys **47**(4) (Jul 2000) 1097–103
2. Jaffray, D., Siewerdsen, J., Wong, J., Martinez, A.: Flat-panel cone-beam computed tomography for image-guided radiation therapy. Int J Radiat Oncol Biol Phys **53** (2002) 1337– 1349
3. Kriminski, S.A., Lovelock, D.M., Seshan, V.E., Ali, I., Munro, P., Amols, H.I., Fuks, Z., Bilsky, M., Yamada, Y.: Comparison of kilovoltage cone-beam computed tomography with megavoltage projection pairs for paraspinal radiosurgery patient alignment and position verification. Int J Radiat Oncol Biol Phys **71**(5) (2008) 1572–80
4. Zhang, Q., Hu, Y.C., Liu, F., Goodman, K., Rosenzweig, K.E., Mageras, G.S.: Correction of motion artifacts in cone-beam ct using a patient-specific respiratory motion model. Medical physics **37**(6) (2010) 2901–2910
5. Reinhardt, J., Christensen, G., Hoffman, E., Ding, K., Cao, K.: Registration-Derived estimates of local lung expansion as surrogates for regional ventilation. Information Processing in Medical Imaging (2007) 763–774
6. Ehrhardt, J., Werner, R., Schmidt-Richberg, A., Schulz, B., Handels, H.: Generation of a mean motion model of the lung using 4D CT image data. Eurographics Workshop on Visual Computing for Biomedicine (2008) 69–76
7. Zhang, Q., Pevsner, A., Hertanto, A., Hu, Y., Rosenzweig, K., Ling, C., Mageras, G.: A patient-specific respiratory model of anatomical motion for radiation treatment planning. Medical Physics **34** (2007) 4772–4781
8. Liu, X., Saboo, R.R., Pizer, S.M., Mageras, G.S.: A shape-navigated image deformation model for 4D lung respiratory motion estimation. IEEE International Symposium on Biomedical Imaging: From Nano to Macro (ISBI) (2009) 875–878
9. Liu, X., Oguz, I., Pizer, S.M., Mageras, G.S.: Shape-correlated deformation statistics for respiratory motion prediction in 4D lung. SPIE Medical Imaging **7625** (2010)
10. Davis, B.C., Fletcher, P.T., Bullitt, E., Joshi, S.C.: Population shape regression from random design data. IEEE International Conference of Computer Vision (ICCV'07) (2007) 1–7
11. Oguz, I., Cates, J., Fletcher, T., Whitaker, R., Cool, D., Aylward, S., Styner, M.: Cortical correspondence using entropy-based particle systems and local features. IEEE International Symposium on Biomedical Imaging: From Nano to Macro (ISBI) (2008) 1637–1640
12. Segars, W., Lalush, D., Tsui, B.: Modeling respiratory mechanics in the MCAT and spline-based MCAT phantoms. IEEE Transactions on Nuclear Science **48**(1) (2001) 89–97